# Low-lying electric-dipole strengths of Ca, Ni, and Sn isotopes imprinted on total reaction cross sections

W. Horiuchi,[1] S. Hatakeyama,[1] S. Ebata,[2] and Y. Suzuki[3,4]

[1]*Department of Physics, Hokkaido University, Sapporo 060-0810, Japan*
[2]*Nuclear Reaction Data Centre, Faculty of Science, Hokkaido University, Sapporo 060-0810, Japan*
[3]*Department of Physics, Niigata University, Niigata 950-2181, Japan*
[4]*RIKEN Nishina Center, Wako 351-0198, Japan*

Low-lying electric-dipole ($E1$) strength of a neutron-rich nucleus contains information on neutron-skin thickness, deformation, and shell evolution. We discuss the possibility of making use of total reaction cross sections on $^{40}$Ca, $^{120}$Sn, and $^{208}$Pb targets to probe the $E1$ strength of neutron-rich Ca, Ni, and Sn isotopes. They exhibit large enhancement of the $E1$ strength at neutron number $N > 28$, 50, and 82, respectively, due to a change of the single-particle orbits near the Fermi surface participating in the transitions. The density distributions and the electric-multipole strength functions of those isotopes are calculated by the Hartree-Fock+BCS and the canonical-basis-time-dependent-Hartree-Fock-Bogoliubov methods, respectively, using three kinds of Skyrme-type effective interaction. The nuclear and Coulomb breakup processes are respectively described with the Glauber model and the equivalent photon method in which the effect of finite-charge distribution is taken into account. The three Skyrme interactions give different results for the total reaction cross sections because of different Coulomb breakup contributions. The contribution of the low-lying $E1$ strength is amplified when the low-incident energy is chosen. With an appropriate choice of the incident energy and target nucleus, the total reaction cross section can be complementary to the Coulomb excitation for analyzing the low-lying $E1$ strength of unstable nuclei.

## I. INTRODUCTION

Electric-dipole ($E1$) excitations of nuclei provide useful information on not only the ground-state properties but also the dipole excitation mechanism. In neutron-rich nuclei, the low-lying $E1$ strength, so-called pygmy dipole resonance, has attracted much attention. In particular, the correlation between the low-lying $E1$ mode and neutron-skin thickness has intensively been discussed in relation to the equation of state of asymmetric nuclear matter [1–3].

The $E1$ excitation mechanism in the neutron-rich unstable nuclei has not yet reached a universal understanding. Recent systematic analyses of the $E1$ strength show that its enhancement strongly depends on the shell structure and mass region [4–6]. A relationship with the so-called "soft" dipole mode due to the excess neutrons and a core nucleus [7–9] is also an interesting subject as a characteristic excitation mode in the neutron-rich unstable nuclei (see recent papers [10,11] and references therein).

Experimental studies of the low-lying $E1$ strength have been performed by using both photoabsorption reactions with real photons and Coulomb breakup reactions with virtual photons generated by a highly charged target nucleus. The former cannot be applied to short-lived unstable nuclei, while the latter can be applied in the inverse kinematics and has often been utilized to extract the low-lying $E1$ strength of halo nuclei [12,13]. Since a weakly bound halo nucleus breaks mainly through the $E1$ transition, the $E1$ strength function is extracted by subtracting the nuclear contribution from one- or two-neutron removal cross sections. We cannot apply this idea for our purpose because most of unstable nuclei are more tightly bound than the halo nuclei. Higher multipole excitations other than $E1$ can also be expected to play a significant role. Furthermore, for the calculation of the nucleon-removal cross sections, we have to assume appropriate final-state wave functions, leading to some ambiguity (see, e.g., Refs. [14,15]).

Inclusive observables that require no final-state wave functions are desired to probe the low-lying $E1$ strength. The total reaction or interaction cross sections measured at medium- to high-incident energies at $\sim$100–1000 $A$ MeV are possible candidates for that purpose. They have been so far used primarily to study nuclear sizes thanks to the following advantages: The measurement is easier and applicable to almost all nuclei, and theoretical models to evaluate the cross sections are well established. The cross sections for stable and unstable nuclei have been measured using light targets, e.g., $^{1}$H and $^{12}$C, because the Coulomb breakup contribution can be negligible. The measurement reaches a few % accuracy for unstable nuclei [16–19], and thus we can discuss structure problems including, for example, deformation [20–24] and neutron-skin thickness [25,26].

In the above measurement of the reaction and interaction cross sections the target nucleus is chosen to be light enough to enable one to neglect the Coulomb breakup contribution [26]. In this paper, we take an opposite direction: We instead consider a heavy target in which the reaction includes large Coulomb breakup contributions, and discuss the possibility of extracting the low-lying $E1$ strength using the total reaction cross section. This is challenging in that the Coulomb breakup contribution has to be evaluated by a sound theory.

The Coulomb breakup process in the high-energy collision is well approximated with the equivalent-photon method

(EPM) [27–29]. It is based on a semiclassical picture in which a relativistic charged particle passes through the Coulomb field produced by the highly charged target nucleus. If the Coulomb excitation is dominated by the $E1$ process, the Coulomb breakup cross section is simply obtained by multiplying the number of the virtual photons and the $E1$ strength functions. The energy dependence of the number of the virtual photons is important: At the high-incident energy $\sim 1000$ MeV/nucleon, the number of the virtual photons distributes from the low-lying to the giant resonance energy region. With the decrease of the incident energy, the virtual photons are concentrated at the low energy region and therefore the contribution of the low-lying strength function to the Coulomb breakup cross sections will be more enhanced. The EPM has been employed to extract the structure of halo nuclei from the low-lying $E1$ strength [12,13]. Reasonable agreement between theory and recent experiment is obtained [13,30] and its validity is studied by reaction calculations [31,32]. We will make use of this sensitivity for extracting the low-lying $E1$ strength of unstable nuclei.

In this paper, we take up Ca, Ni, and Sn isotopes with even neutron numbers $N = 20$–40 for Ca, 28–56 for Ni, and 50–90 for Sn, because the enhancement of the low-lying $E1$ strength is predicted at $N > 28$, 50, 82 for Ca, Ni, and Sn isotopes, respectively [4]. At those magic numbers, $0f_{7/2}$, $0g_{9/2}$, and $0h_{11/2}$ neutron orbits are fully occupied, respectively. The higher major shell orbits play a vital role to determine the $E1$ strength. A sudden increase of the $E1$ strength is clearly seen in "PDR fraction" [4], which is defined as a fraction of total and cumulative energy-weighted sums up to *ad hoc* cut-off excitation energy, 10 MeV. The enhancement in fact strongly depends on the interaction employed or very sensitive to the single-particle structure near the Fermi surface. We investigate the total reaction cross sections including the Coulomb multipole excitations in order to answer whether they can be used as a probe of the low-lying $E1$ strength. This study provides us with information on the shell structure beyond the magic numbers $N = 28$, 50, 82 of neutron-rich nuclei and can also be a strong test of the Skyrme interaction employed. The role of the low-lying $E1$ strength is quantified in the Coulomb breakup contribution as well as the contributions from other electric multipoles. Incident energy and target dependence of the total reaction cross sections are systematically analyzed.

In the next section, we describe our reaction and structure models as well as a way to include the Coulomb multipole effects into the cross section. Since we consider highly charged particles, a finite size effect of the target charge distribution, which is usually ignored in the EPM, is also formulated in this section. Numerical results are presented in Sec. III, mainly focusing on Sn isotopes. In Sec. III A, we first discuss the effect of the finite charge distribution in the EPM. In Sec. III B, we make a systematical analysis of the total reaction cross sections of Sn isotopes. The contributions of the Coulomb multipole excitations are quantified in Sec. III C. We discuss in Sec. III D the incident energy and target dependence of the total reaction cross section and its sensitivity to the $E1$ strength. In Sec. III E, we show the total reaction cross sections of Ca and Ni isotopes. Conclusions are given in Sec. IV.

## II. TOTAL REACTION CROSS SECTION

We consider the total reaction cross section ($\sigma_R$) on a heavy target that induces a large amount of Coulomb excitations. The total reaction cross section is expressed as a sum of the nuclear breakup cross section ($\sigma_N$) and the Coulomb breakup cross section ($\sigma_C$):

$$\sigma_R = \sigma_N + \sigma_C. \qquad (1)$$

See, e.g., Refs. [26,33] for its validity. The nuclear and Coulomb interference term is negligibly small. These cross sections are calculated as explained below.

### A. Nuclear breakup

The $\sigma_N$ is calculated in the Glauber formalism [34] by

$$\sigma_N = \int d\boldsymbol{b} \, (1 - |e^{i\chi(\boldsymbol{b})}|^2), \qquad (2)$$

where $\boldsymbol{b}$ is the impact parameter vector perpendicular to the beam direction. The nuclear optical phase-shift function, $\chi(\boldsymbol{b})$, contains all information of the high-energy nuclear collision. We calculate $\chi(\boldsymbol{b})$ in the nucleon-target formalism in the Glauber theory [35], which is known to give a better description of high-energy nucleus-nucleus collisions than the ordinary optical-limit approximation. It is easily calculated by using the ground state densities of both the projectile and target nuclei and the parameters of the profile function describing the $NN$ collision are taken from Ref. [36]. The present method for computing $\sigma_N$ has been successfully applied to many examples of nucleus-nucleus collisions including light unstable nuclei [21,30,37–39].

We use the ground-state density distributions of Ca, Ni, and Sn isotopes and the target nuclei, $^{40}$Ca, $^{120}$Sn, and $^{208}$Pb obtained in Ref. [26], where the Hartree-Fock (HF)+BCS method is applied to three kinds of the Skyrme-type effective interaction, SkM* [40], SLy4 [41], and SkI3 [42]. We employ a constant monopole pairing as in Refs. [4,43], where the level density determining its pairing strength is calculated by each of the Skyrme interactions. Once all the inputs are set, the calculation of $\sigma_N$ contains no adjustable parameter.

### B. Coulomb breakup

To calculate $\sigma_C$ we have to consider some basic elements such as equivalent photon method (EPM), photoabsorption cross sections, and effect of finite charge distribution. These are discussed below.

#### 1. Multipole excitations by virtual photons

We consider the Coulomb breakup probability $P_C(\boldsymbol{b})$ according to the EPM [27–29]. The Coulomb breakup occurs through both electric- and magnetic-multipole excitations, but the latter contribution is ignored in this paper because a ratio of the photon-number spectra of $E1$ and $M1$ transitions is roughly proportional to $(v/c)^4$ [27], and the $M1$ strength is in general much smaller than the $E1$ strength [44]. $P_C(\boldsymbol{b})$ is given as a sum of electric multipoles labeled by $\lambda$, and each multipole is obtained by the equivalent photon number $N_{E\lambda}(\boldsymbol{b}, \omega)$ multiplied by the photoabsorption cross section

$\sigma_{E\lambda}(\omega)$ integrating over the frequency $\omega$:

$$P_C(\boldsymbol{b}) = \sum_\lambda \int_0^\infty d\omega\, N_{E\lambda}(\boldsymbol{b},\omega)\sigma_{E\lambda}(\omega). \tag{3}$$

Assuming point-charge distribution of the target nucleus, the multipole decomposition of the photon numbers per unit area per unit frequency is given by [27]

$$N_{E\lambda}(\boldsymbol{b},\omega) = Z_T^2\alpha\frac{\lambda[(2\lambda+1)!!]^2}{(2\pi)^3(\lambda+1)}\sum_m |G_{E\lambda m}(\xi)|^2\frac{\xi^2}{\omega b^2}K_m^2(\xi) \tag{4}$$

with

$$G_{E\lambda m}(x) = i^{\lambda+m}\frac{\sqrt{16\pi}}{\lambda(2\lambda+1)!!}\left\{\frac{(\lambda+1)(\lambda+m)}{2\lambda+1}P_{\lambda-1}^m(x)\right.$$
$$\left. -\frac{\lambda(\lambda-m+1)}{2\lambda+1}P_{\lambda+1}^m(x)\right\}, \tag{5}$$

where $\alpha$ is the fine structure constant and $\xi = b\omega/\gamma v$ with the Lorentz factor $\gamma = 1/\sqrt{1-(v/c)^2}$. $K_m$ is the modified Bessel function of the second kind and $P_l^m$ is the associated Legendre polynomial.

### 2. Mean-field calculations for photoabsorption cross sections

The nuclear structure information of the Coulomb breakup reaction is contained in $\sigma_{E\lambda}(\omega)$, which is related to the $E\lambda$ strength (response) function $S(E\lambda;\omega)$ as

$$\sigma_{E\lambda}(\omega) = \frac{(2\pi)^3(\lambda+1)}{\lambda[(2\lambda+1)!!]^2}\omega^{2\lambda-1}S(E\lambda;\omega). \tag{6}$$

The canonical-basis-time-dependent-HF-Bogoliubov method is employed to obtain $S(E\lambda;\omega)$ [45]. A linear response by the $E\lambda$ field is obtained using the prescription given in Ref. [46]. The initial state is generated by applying a weak impulse field to the ground state:

$$F_K^{E1} = \begin{cases} e(N/A)rY_{1K}(\hat{\boldsymbol{r}}), & \text{(for proton)} \\ -e(Z/A)rY_{1K}(\hat{\boldsymbol{r}}), & \text{(for neutron)} \end{cases} \tag{7}$$

$$F_K^{E\lambda} = e\frac{r^\lambda Y_{\lambda K}(\hat{\boldsymbol{r}}) + r^\lambda Y_{\lambda-K}(\hat{\boldsymbol{r}})}{\sqrt{2(1+\delta_{K0})}}, \quad \text{(for proton, } \lambda > 1\text{)} \tag{8}$$

and the time evolution of the initial state enables us to obtain the strength function.

### 3. Equivalent photon method with finite-charge distribution

If the target nucleus is treated as a point-charged particle with charge $Z_T e$, the number of equivalent photons at the center of mass ($\boldsymbol{r} = 0$) of the fast-moving projectile nucleus with velocity $v$ is obtained by using the electric field $\boldsymbol{E}(\boldsymbol{r},\omega)$ as [27,28]

$$N(\boldsymbol{b},\omega) = \frac{c}{\hbar\omega}|\boldsymbol{E}(\boldsymbol{r},\omega)|_{\boldsymbol{r}=0}^2$$
$$= \frac{Z_T^2\alpha}{\pi^2}\left(\frac{c}{v}\right)^2\frac{\xi^2}{\omega b^2}\left[K_1^2(\xi) + \frac{1}{\gamma^2}K_0^2(\xi)\right]. \tag{9}$$

As was done in Ref. [27], the multipole decomposition of the electric field is possible by considering $\boldsymbol{r}$-dependence but we

discuss the electric field at the origin $\boldsymbol{r} = 0$ in this paper for the sake of simplicity. Note that $N_{E1}(\boldsymbol{b},\omega)$ of Eq. (4) is equal to $N(\boldsymbol{b},\omega)$.

The target nuclei considered in this paper are medium and heavy nuclei, and it is appropriate to discuss possible deviation from the point-charge approximation. In the following we estimate the extent to which $N(\boldsymbol{b},\omega)$ of Eq. (9) changes for the finite charge distribution. Let $Z_T e\rho_T(\boldsymbol{r}')$ denote the charge density of the target nucleus, $\int d\boldsymbol{r}'\rho_T(\boldsymbol{r}') = 1$. The electric field produced by the fast moving target nucleus is

$$\boldsymbol{E}(\boldsymbol{r},t)|_{\boldsymbol{r}=0} = -Z_T e\int d\boldsymbol{r}'\frac{\boldsymbol{R}(t)}{\gamma^2 u^3}\rho_T(\boldsymbol{r}'), \tag{10}$$

where, with $\boldsymbol{r}' = (\boldsymbol{s}',z')$,

$$\boldsymbol{R}(t) = \boldsymbol{b} + \boldsymbol{v}t + \boldsymbol{s}' - \frac{\boldsymbol{v}}{v}z',$$
$$u = \sqrt{\frac{1}{\gamma^2}(\boldsymbol{b}+\boldsymbol{s}')^2 + (vt-z')^2}. \tag{11}$$

The center-of-mass of the target nucleus is assumed to move along the $-z$ direction with the velocity $\boldsymbol{v} = (0,0,-v)$ and each nucleon of the target nucleus is also assumed to follow a straight-line trajectory. The above field can be considered a superposition of fields with various frequencies.

A Fourier analysis of the electric field gives

$$\boldsymbol{E}(\boldsymbol{r},\omega)|_{\boldsymbol{r}=0} = \frac{1}{2\pi}\int_{-\infty}^{+\infty}dt\,e^{i\omega t}\boldsymbol{E}(\boldsymbol{r},t)|_{\boldsymbol{r}=0}. \tag{12}$$

Performing $t$-integration with Eq. (10) leads to

$$\boldsymbol{E}(\boldsymbol{r},\omega)|_{\boldsymbol{r}=0} = -\frac{Z_T e\xi}{\pi bv}\int d\boldsymbol{r}'e^{i\frac{\omega}{v}z'}\rho_T(\boldsymbol{r}')$$
$$\times\left[\hat{\boldsymbol{p}}K_1(p) + i\frac{\hat{\boldsymbol{v}}}{\gamma}K_0(p)\right], \tag{13}$$

where $\hat{\boldsymbol{v}} = \boldsymbol{v}/v$ and

$$\boldsymbol{p} = \xi\left(\hat{\boldsymbol{b}} + \frac{1}{b}\boldsymbol{s}'\right). \tag{14}$$

The number of equivalent photons modified by the finite charge distribution is obtained as

$$\tilde{N}(\boldsymbol{b},\omega) = \frac{Z_T^2\alpha}{\pi^2}\left(\frac{c}{v}\right)^2\frac{\xi^2}{\omega b^2}$$
$$\times\left[\tilde{\boldsymbol{K}}_1(\xi,\omega)\cdot\tilde{\boldsymbol{K}}_1(\xi,\omega) + \frac{1}{\gamma^2}\tilde{K}_0^2(\xi,\omega)\right], \tag{15}$$

where

$$\tilde{\boldsymbol{K}}_1(\xi,\omega) = \int d\boldsymbol{r}'e^{i\frac{\omega}{v}z'}\rho_T(\boldsymbol{r}')\hat{\boldsymbol{p}}K_1(p),$$
$$\tilde{K}_0(\xi,\omega) = \int d\boldsymbol{r}'e^{i\frac{\omega}{v}z'}\rho_T(\boldsymbol{r}')K_0(p). \tag{16}$$

Here, $\rho_T(\boldsymbol{r}')$ is assumed to be invariant with respect to the reflection of $z' \to -z'$, which guarantees that both $\tilde{\boldsymbol{K}}_1(\xi,\omega)$ and $\tilde{K}_0(\xi,\omega)$ are real. The integration in Eq. (16) is easily performed by expanding $\rho_T(\boldsymbol{r})$ in terms of a sum of Gaussians. See Appendix for details. The ratio, $r(\boldsymbol{b},\omega) = \tilde{N}(\boldsymbol{b},\omega)/N(\boldsymbol{b},\omega)$,

gives the change of the photon-number spectrum as a function of $b$ and $\omega$:

$$r(\boldsymbol{b},\omega) = \frac{\tilde{K}_1(\xi,\omega) \cdot \tilde{K}_1(\xi,\omega) + \frac{1}{\gamma^2}\tilde{K}_0^2(\xi,\omega)}{K_1^2(\xi) + \frac{1}{\gamma^2}K_0^2(\xi)}. \quad (17)$$

At large $\boldsymbol{b}$ that exceeds the charge radius of the target, we numerically find that the ratio has no incident-energy dependence and goes to a constant independent of $b$. Note that $\int_0^\infty d\omega \tilde{N}(\boldsymbol{b},\omega) = \int_0^\infty d\omega N(\boldsymbol{b},\omega)$ holds at large $\boldsymbol{b}$. We will examine $r(\boldsymbol{b},\omega)$ in Sec. III A.

#### 4. Coulomb breakup reaction probability

The Coulomb breakup probability of Eq. (3) is replaced by including the finite-charge distribution as follows:

$$P_C(\boldsymbol{b}) = \sum_\lambda \int_0^\infty d\omega\, r(\boldsymbol{b},\omega) N_{E\lambda}(\boldsymbol{b},\omega)\sigma_{E\lambda}(\omega). \quad (18)$$

Here, we assume that the finite distribution applies equally to all the multipoles. Since the EPM is formulated in a classical way, the probability $P_C(\boldsymbol{b})$ exceeds unity at small $b$. To avoid this unphysical problem, we multiply the Coulomb breakup probability by the survival probability $|e^{i\chi(\boldsymbol{b})}|^2$ of the colliding nuclei [29,47]

$$\sigma_C = \int d\boldsymbol{b}\, P_C(\boldsymbol{b})|e^{i\chi(\boldsymbol{b})}|^2. \quad (19)$$

This ansatz is more natural than introducing a sudden cut-off impact parameter that is usually taken as a sum of the nuclear radii of the projectile and target nuclei.

We have discussed the Coulomb excitations of the projectile nucleus by the target nucleus. We have to consider the other way around, that is, the Coulomb field of the projectile excites the target because a measurement excluding such process can not be possible. As was done in Ref. [26], both the Coulomb breakup cross sections of the projectile and target nuclei are added incoherently to the nuclear breakup cross section. $\sigma_{E\lambda}(\omega)$ of the target nucleus is calculated in exactly the same manner as that of the projectile nucleus. It may be likely that the incoherent sum leads to some overestimation of $\sigma_C$. If mutual excitations of both projectile and target nuclei are considered, it may not be valid to assume that such excited nuclei generate the same photon-number spectrum as the one employed in Eq. (4). Instead, they produce somewhat weaker field each other, leading to the reduced Coulomb breakup cross section.

### III. RESULTS AND DISCUSSIONS

#### A. Comparison of the EPM with point- and finite-charge distributions

To show the effect of the finite-charge distribution in the EPM, we display in Fig. 1 the ratio $r(\boldsymbol{b},\omega)$ at $b = 20$ fm as a function of the excitation energy of the projectile nucleus. For small $\hbar\omega \lesssim 5$ MeV, the point- and finite-charge distributions give almost equal photon numbers. For $\hbar\omega \simeq 10$–$15$ MeV where the giant dipole resonance appears, approximately 5% reduction is obtained for $^{208}$Pb target. With increasing $\omega$ further suppression occurs for a heavier target nucleus. The
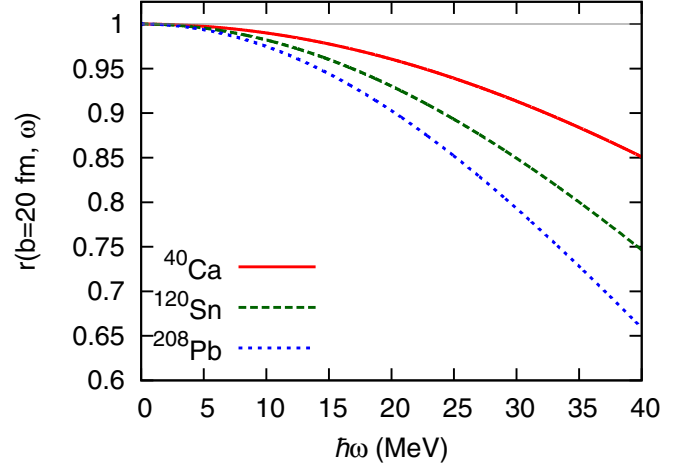


FIG. 1. Ratio of the photon numbers $r(b = 20\,\mathrm{fm},\omega)$ of finite- and point-charge distributions of $^{40}$Ca, $^{120}$Sn, and $^{208}$Pb targets as a function of $\hbar\omega$. See Eq. (17).

calculated Coulomb breakup cross sections of $^{120}$Sn incident at 100–1000 $A$ MeV are reduced by 1–3 %, 3–4 %, 4–5 % for $^{40}$Ca, $^{120}$Sn, and $^{208}$Pb targets, respectively, compared to the case of the point charge. Hereafter we employ the EPM with the finite-charge distribution.

#### B. Systematics of total reaction cross sections

Figure 2 displays $\sigma_R$, $\sigma_N$, and $\sigma_C$ of Sn isotopes incident on (a1)–(a4) $^{40}$Ca, (b1)–(b4) $^{120}$Sn, and (c1)–(c4) $^{208}$Pb targets at the incident energies of 100, 200, 550, and 1000 $A$ MeV. At all incident energies, the cross sections increase as the neutron number increases. All the Skyrme interactions give almost the same results for Ca target because the nuclear breakup contributions dominate. For Sn and Pb targets, the Coulomb contribution increases and the interaction dependence shows up through $\sigma_C$ although $\sigma_N$ is insensitive to the interaction. At the lower-incident energies, the cross sections calculated with the SkM* and SLy4 interactions are almost the same, whereas those with the SkI3 interaction behave differently from the others. At the higher-incident energies, the SkM* and SLy4 interactions give different cross sections. The different behavior of $\sigma_R$ with the incident energy suggests some change of structure on the Sn isotope chain.

Both the nuclear and Coulomb breakup cross sections increase gradually as the neutron number increases. All panels of Fig. 2 show kink behavior at $N = 82$ where the neutron $0h_{11/2}$ orbit is fully occupied. The isotope dependence of $\sigma_N$ is rather moderate, reflecting the increase of its matter radius. The $\sigma_C$ on $^{40}$Ca target also shows smooth dependence on the neutron number, but for $^{120}$Sn and $^{208}$Pb targets it exhibits a rapid increase at $N > 82$. This behavior corresponds to the sudden appearance of the low-lying $E1$ strengths [4].

The enhancement of the low-lying $E1$ strength can be understood by considering the neutron level structure around the Fermi surface. Though the HF+BCS model mixes the single-particle orbits near the Fermi surface, we discuss it with the dominant neutron orbits for the sake of simplicity.
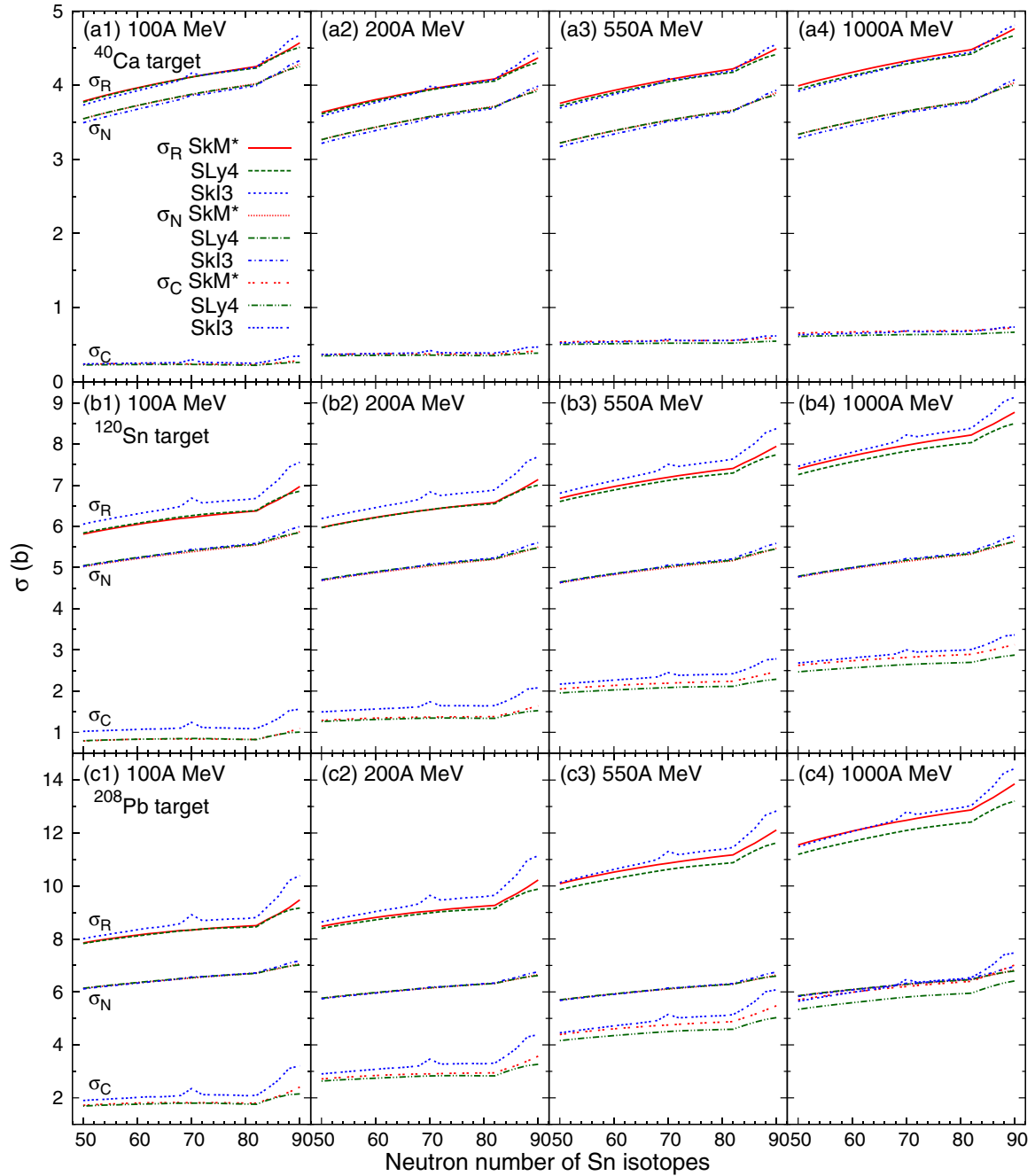
FIG. 2. Total reaction ($\sigma_R$), nuclear breakup ($\sigma_N$), Coulomb breakup ($\sigma_C$) cross sections of Sn isotopes, [100–140]Sn, incident on (a1)–(a4) [40]Ca, (b1)–(b4) [120]Sn, and (c1)–(c4) [208]Pb targets at the incident energies of 100, 200, 550, and 1000 $A$ MeV. The SkM*, SLy4, and SkI3 interactions are employed.

In the mass region of $N = 70$–82, the outermost neutrons are filled in the $0h_{11/2}$ orbit. At $N > 82$, the $1f_{7/2}$ orbit accommodates further neutrons up to $N = 90$. With the SkI3 interaction, the Fermi energy becomes very small, accounting for larger enhancement of the low-lying $E1$ strength at $N > 82$, compared to those with the SkM* and SLy4 interactions (see Ref. [4] or Fig. 5 in Sec. III D).

This excitation mechanism is similar to that found in [22]C [11] in which the $E1$ strength is governed by the single-particle excitations from the outermost $sd$ orbits, $1s_{1/2}$

and $0d_{5/2}$, which are energetically almost degenerate. The enhancement of the $E1$ strength is found as the Fermi energy decreases due to the spatial extension of the $sd$ orbits. In case of [134]Sn, the root-mean-square (rms) radii of the outermost single-particle orbit, $1f_{7/2}$, are 5.96, 6.13, and 6.44 fm with the SkM*, SLy4, and SkI3 interactions, respectively. The rms radius with the SkI3 interaction extends very much compared to the others, accounting for the large enhancement of the low-lying $E1$ strength at $N = 84$. The corresponding single-particle energies are $-3.21$, $-2.15$, and $-1.53$ MeV for SkM*,
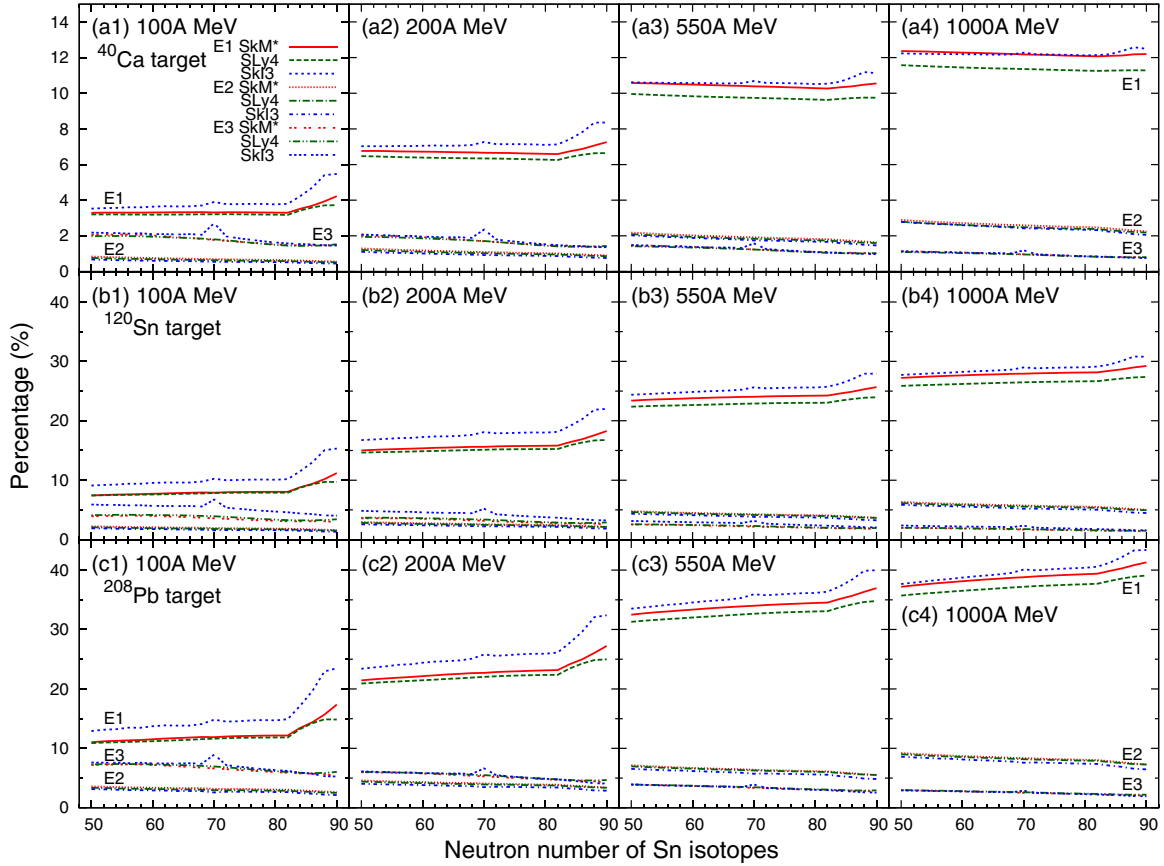
FIG. 3. Percentages of the Coulomb breakup cross sections with electric multipoles, $E1, E2$, and $E3$, in the total reaction cross sections of Sn isotopes, $^{100-140}$Sn, incident on (a1)–(a4) $^{40}$Ca, (b1)–(b4) $^{120}$Sn, and (c1)–(c4) $^{208}$Pb targets at the incident energies of 100, 200, 550, and 1000 $A$ MeV. The SkM*, SLy4, and SkI3 interactions are employed.

SLy4, and SkI3 interactions, respectively. The rms radius is well correlated with the single-particle energy. In contrast, the rms radius of the fully occupied $0h_{11/2}$ orbit in $^{134}$Sn remains at almost the same values: 5.57, 5.61, and 5.67 fm with the SkM*, SLy4, and SkI3 interactions, respectively. Since those neutrons are deeply bound at $-7.8$ to $-8.6$ MeV and the radii do not change drastically at $N \leqslant 82$, the interaction dependence of the low-lying $E1$ strength is small at $N \leqslant 82$.

A bump of $\sigma_C$ at $N = 70$ appears only with the SkI3 interaction, and it is due to an increase of the $E3$ strength function. Pairing correlations always play a role of suppressing a sudden structure change with increasing neutron number [26]. The pairing effect actually vanishes at $N = 70$ for the SkI3 interaction, giving the sudden increase of the $E3$ cross section.

It should be noted that $\sigma_C$ becomes very large and comparable to $\sigma_N$ especially for large-$Z$ targets at high incident energies because of the increase of the photon numbers (4). With $^{208}$Pb target, the $\sigma_C$ is almost equal to $\sigma_N$ at incident energies higher than $\sim 500A$ MeV. This suggests that the information of the $E\lambda$ strength function can be observed by measuring $\sigma_R$ at different combinations of the incident energy and the target nucleus.

### C. Coulomb multipole excitations

The Coulomb multipole excitations are expected to play an important role in particular at the low-incident

energies [26,27]. To quantify the contribution of each multipole, we plot in Fig. 3 the percentage of $E\lambda$ Coulomb breakup cross section compared to the total reaction cross section. The $E1$ contributions are dominant for all cases although their percentages depend on the choice of the Skyrme interaction, target, and incident energy. At $N = 82$, we see kink behavior which becomes more evident as the incident energy is lowered. The $E2$ and $E3$ percentages show almost constant behavior and do not so much depend on the neutron number. The $E3$ contribution is even larger than the $E2$ contribution when the Sn isotopes are incident on $^{40}$Ca, $^{120}$Sn, and $^{208}$Pb targets at the incident energies of 100 and 200 $A$ MeV. This can be explained by the following two factors: In spherical nuclei, the low-lying $E2$ strengths are suppressed [48,49]. In fact, all Sn isotopes considered in this paper have a spherical shape [4,26]. The second is the behavior of the photon-number spectrum which will be discussed in Sec. III D. At the high-incident energies, the $E2$ and $E3$ contributions are small, approximately one order of magnitude smaller than the $E1$ contribution. As the incident energy decreases, the $E2$ and $E3$ contributions compared to the $E1$ become larger. In the case of $^{208}$Pb target at $100A$ MeV, the contribution of the higher multipole excitations is comparable to that of $E1$. Although the isotope dependence of the total reaction cross sections is dominated by the $E1$ contributions, the higher multipole contributions have to be included for a quantitative
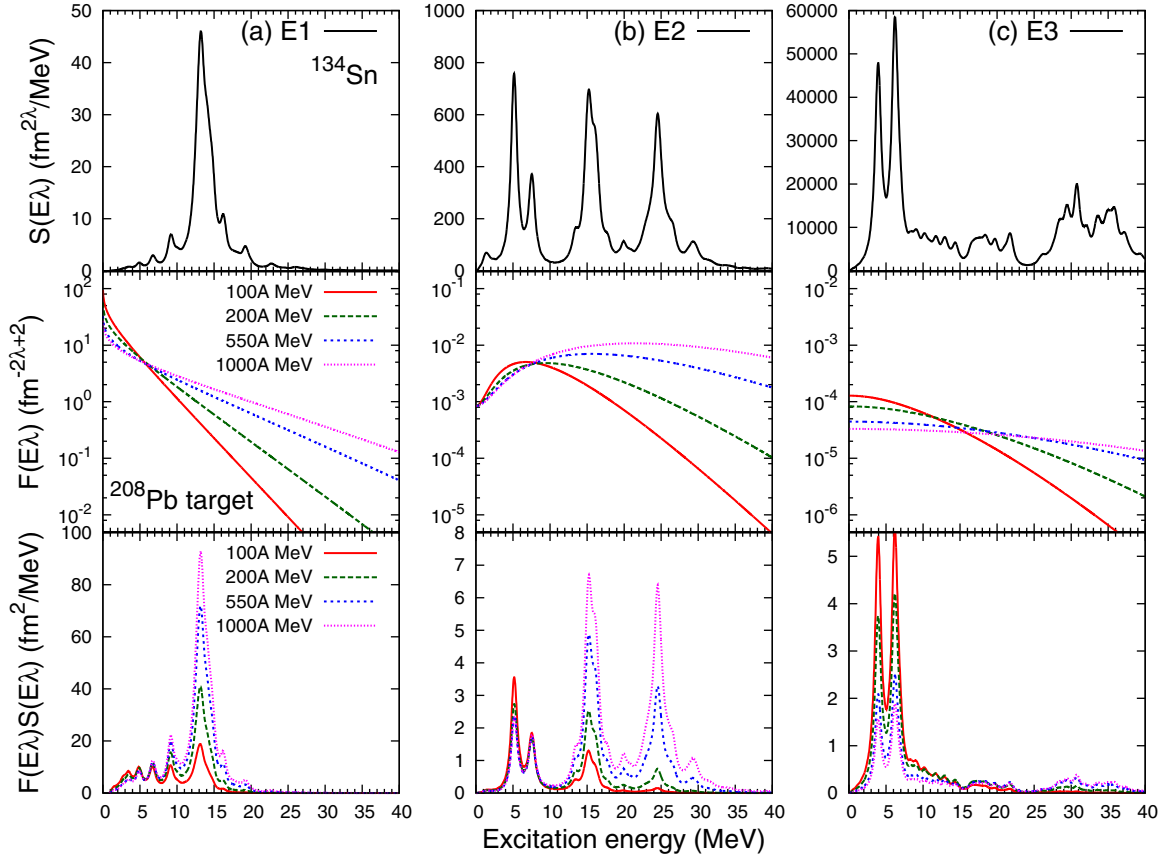
FIG. 4. Contributions of the electric-multipole strengths of $^{134}$Sn to the Coulomb breakup cross section ($\sigma_C$) by $^{208}$Pb target as a function of the excitation energy: (a) $E1$, (b) $E2$, and (c) $E3$. See Eqs. (20) and (21). The weight function $F(E\lambda)$ is plotted at the incident energies of 100, 200, 550, and 1000 $A$ MeV. The SkI3 interaction is employed.

evaluation of the cross sections, especially at the low-incident energy.

To test the validity of our approach, we compare theory with measurement. Only few experimental data of the total reaction cross section involving heavy projectile and target nuclei are available in literature. The total reaction cross sections of $^{118}$Sn $+$ $^{40}$Ca and $^{208}$Pb $+$ $^{40}$Ca collisions incident at $77 A$ MeV are tested. The $\sigma_R$ ($\sigma_C$) values calculated with the SkM*, SLy4, and SkI3 interactions are, in units of barn, 4.20 (0.23), 4.20 (0.22), and 4.18 (0.24) for $^{118}$Sn $+$ $^{40}$Ca, and 5.46 (0.47), 5.43 (0.45), and 5.47 (0.52) for $^{208}$Pb $+$ $^{40}$Ca, respectively. The interaction dependence is negligibly small. The corresponding experimental $\sigma_R$ values are $4.89 \pm 0.53$ and $5.33 \pm 0.50$ [50], in fair agreement with the theoretical ones. The theoretical cross sections may be further improved by including higher multipole contributions ($\lambda > 3$) as the incident energy is low.

### D. Coulomb breakup and $E\lambda$ strength functions

All discussions in the previous subsection can be understood by making explicit the nuclear structure information contained in the Coulomb breakup cross section. For this purpose, we rewrite $\sigma_C$ of Eq. (19) as an integral of the $E\lambda$ strength function, $S(E\lambda; \omega)$, over the excitation (photon) energy:

$$\sigma_C = \sum_\lambda \int_0^\infty d\omega \, F(E\lambda; \omega) S(E\lambda; \omega), \qquad (20)$$

where the weight function $F(E\lambda; \omega)$ contains the dynamical aspect of the Coulomb breakup reaction, especially the equivalent photon numbers:

$$F(E\lambda; \omega) = \frac{(2\pi)^3(\lambda + 1)}{\lambda[(2\lambda + 1)!!]^2}\omega^{2\lambda-1}$$

$$\times \int d\boldsymbol{b}\, r(\boldsymbol{b}, \omega) N_{E\lambda}(\boldsymbol{b}, \omega)|e^{i\chi(\boldsymbol{b})}|^2. \qquad (21)$$

The expression of $\sigma_C$ as an integral over $\omega$ is more natural than that over $\boldsymbol{b}$. This is because the Coulomb breakup occurs even at large impact parameter due to the fact that the Coulomb force is long-ranged and rather we are interested in the nuclear response as a function of the excitation energy.

Figure 4 plots $S(E\lambda)$, $F(E\lambda)$, and their product $F(E\lambda)S(E\lambda)$, $E\lambda$ Coulomb breakup cross section per unit energy, as a function of $\omega$ for the Coulomb breakup of $^{134}$Sn ($N = 84$) by $^{208}$Pb target. The SkI3 interaction is employed. For the sake of simplicity, only the excitation of $^{134}$Sn is taken into account, whereas the contribution of the $^{208}$Pb excitation is ignored. The $S(E1)$ exhibits the so-called pygmy dipole resonance below 10 MeV and the giant dipole resonance peak at around 13 MeV. The $E1$ weight function $F(E1)$ decreases rapidly as the excitation energy increases. As the incident energy increases, the falloff of $F(E1)$ with the excitation energy becomes more gentle because of the increase of the
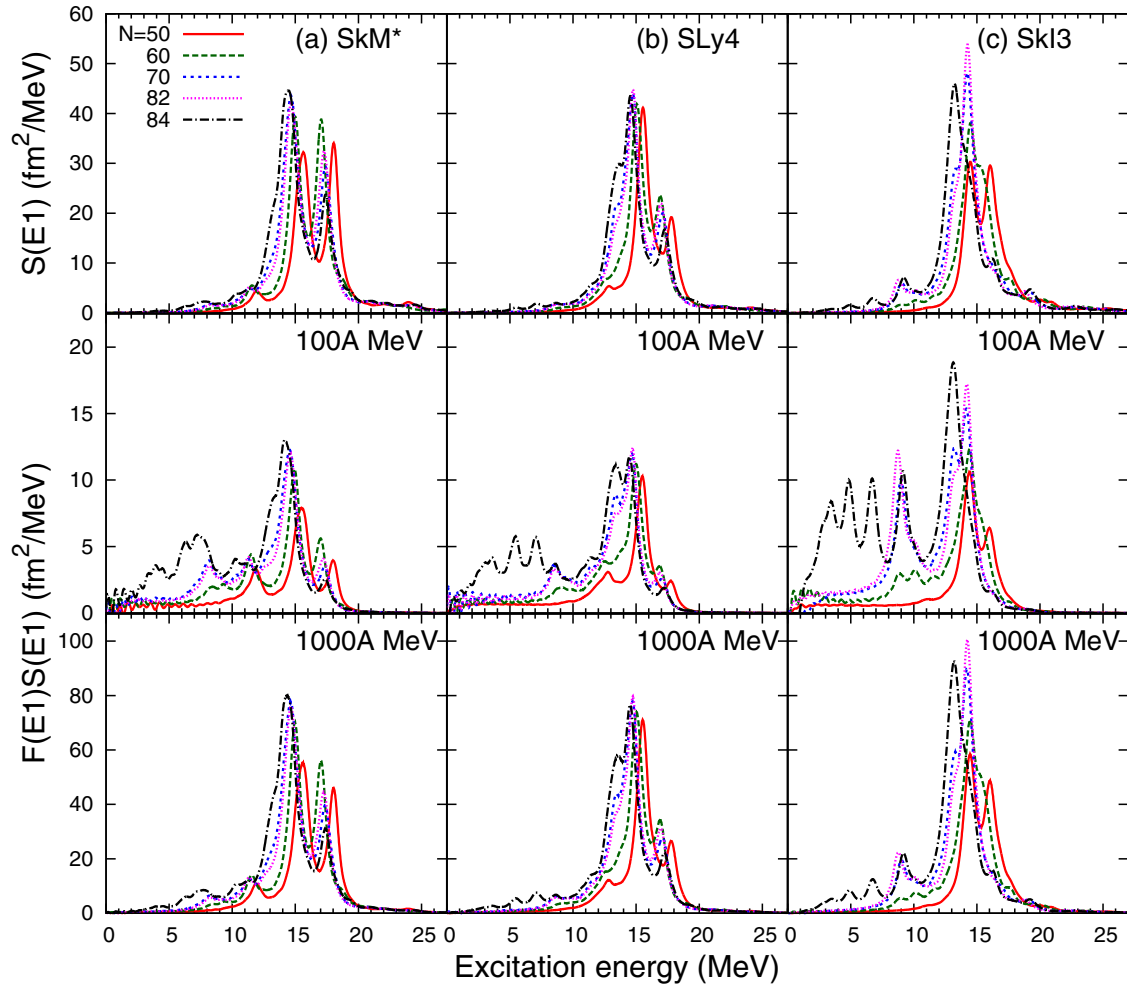
FIG. 5. Comparison of the electric-dipole ($E1$) contributions of Sn isotopes, $^{100,110,120,132,134}$Sn, to the Coulomb breakup cross sections by $^{208}$Pb target. The $E1$ strength functions $S(E1)$ are plotted as a function of the excitation energy for three Skyrme interactions, (a) SkM*, (b) SLy4, and (c) SkI3, and for each case two incident energies of $100A$ and $1000A$ MeV are chosen to draw the Coulomb breakup cross sections per unit energy $F(E1)S(E1)$.

photon number. The $E1$ Coulomb breakup cross section per unit energy, $F(E1)S(E1)$, does not depend on the incident energies at low excitation energies up to about 7 MeV, while it is enhanced with the increasing incident energy in the giant dipole resonance region. The excitation-energy dependence of the $E1$ Coulomb breakup cross section at $1000A$ MeV is similar to that of $S(E1)$. The Coulomb breakup cross section at the high-incident energy can therefore be a probe of the nonenergy weighted $E1$ sum rule, which is closely related to the radii of the proton distribution [44,51].

We turn to the $E2$ contribution. $S(E2)$ shows some low-lying peaks at about 5 MeV and two large peaks at the higher energy region, while $F(E2)$ has almost no vital dependence on the incident energy up to 10 MeV but becomes larger and larger beyond 10 MeV as the incident energy increases. Thus the $E2$ cross section increases with the increase of the incident energy. Since the $E2$ strengths are suppressed in spherical Sn isotopes and therefore $F(E2)S(E2)$ is small, the $E2$ contribution to $\sigma_C$ is much smaller than $E1$.

In the $E3$ case, $F(E3)S(E3)$ at the low excitation energy becomes smaller and smaller with increasing incident energy,

in contrast to the $E1$ and $E2$ cases. This is understood from the excitation-energy dependence of $F(E3)$. This specific energy dependence plays a role in enhancing the $E3$ contribution at the low-incident energy as displayed in Fig. 3.

Since the $E1$ contributions dominate in $\sigma_C$, it is interesting to examine the extent to which $S(E1)$ and $F(E1)S(E1)$ change with the neutron number. Figure 5 displays the results of $^{100,110,120,132,134}$Sn calculated with the three Skyrme interactions. The low-lying $E1$ strength contributes significantly to the reaction probability at the low-incident energy because the photon numbers or $F(E1; \omega)$ concentrate at the low-energy region. At $100A$ MeV the low-lying strength is significantly enhanced compared to that in the giant dipole resonance region, while at $1000A$ MeV no such enhancement occurs and the reaction probability distribution is similar to that of the $E1$ strength distribution. Since the photon number in the low-excitation energy region becomes large at the low-incident energy, the information on the low-lying $E1$ strength can possibly be obtained by a measurement involving the $E1$ Coulomb breakup process at the low-incident energy.
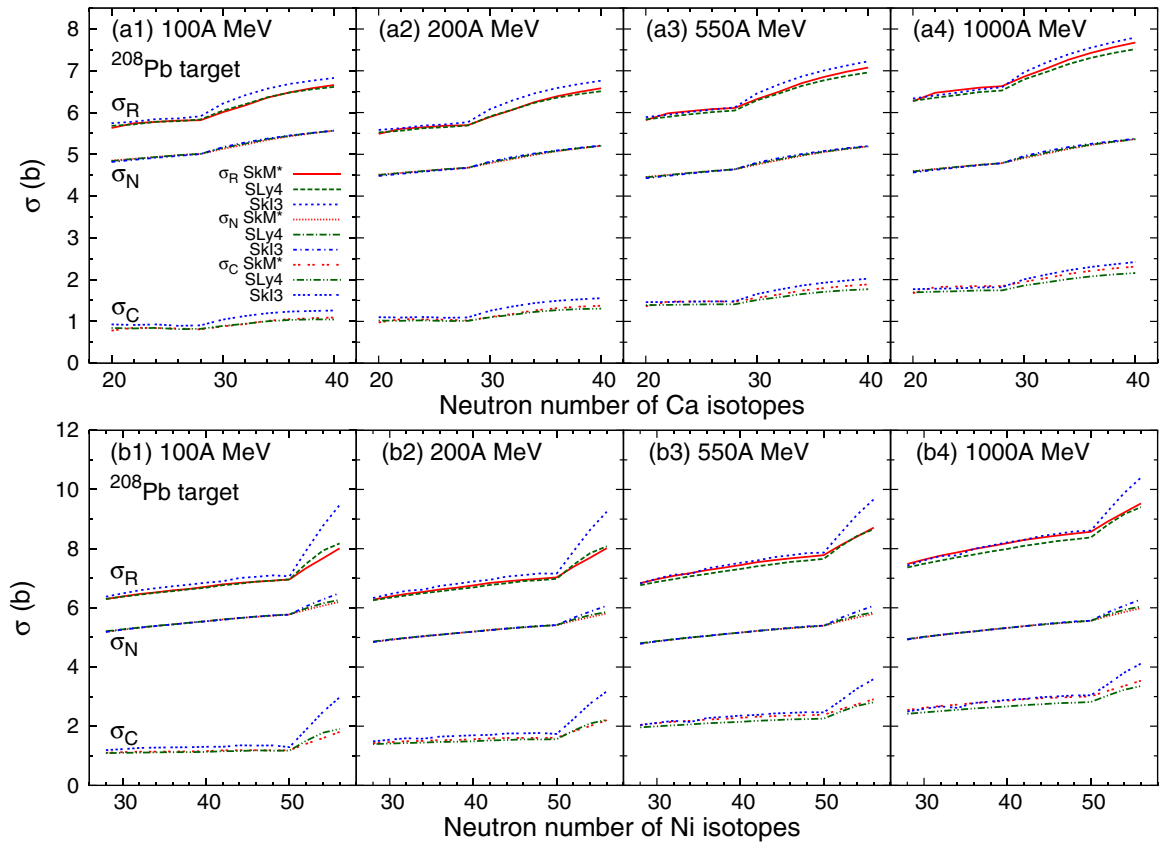
FIG. 6.  Same as Fig. 2 but for (a1)–(a4) $^{40-60}$Ca and (b1)–(b4) $^{56-84}$Ni incident on $^{208}$Pb target.

### E.  Total reaction cross sections of Ca and Ni isotopes

The mechanism of the cross section enhancement in the Ca and Ni isotopes is similar to that of the Sn isotopes but different single-particle orbits are involved. Figure 6 plots the total reaction cross sections of Ca and Ni isotopes incident on $^{208}$Pb target with various incident energies. Though the Coulomb breakup cross sections are not as large as those of Sn isotopes because of smaller-$Z$ values of Ca and Ni isotopes, as expected, large enhancement of the Coulomb breakup cross sections is found at $N > 28$ and $N > 50$ for Ca and Ni isotopes, respectively. The enhancement becomes more prominent with lowering the incident energy. At $N = 28$ ($N = 50$), $0f_{7/2}$ ($0g_{9/2}$) orbit is fully occupied and the weakly bound neutron orbits in the higher major shell play a primarily important role at $N > 28$ ($N > 50$). Similarly to the Sn case, the enhancement is due to sudden changes of the Fermi energies or rms radii of the outermost neutron orbit. For the most prominent case, $^{80}$Ni ($N = 52$), the single-particle energies and rms radii of the dominant outermost orbit, $1d_{5/2}$, are $-2.72, -1.62, -1.31$ MeV, and 5.46, 5.71, and 6.05 fm for the SkM*, SLy4, and SkI3 interactions, respectively. In fact, the SkI3 interaction gives a drastic increase at $N = 52$. For $^{50}$Ca ($N = 30$), those of the outermost $1p_{3/2}$ orbit are $-5.76$, $-6.59$, and $-5.16$ MeV, and 4.60, 4.47, and 4.79 fm for the SkM*, SLy4, and SkI3 interactions, respectively. Since the single-particle energy (radius) of the outermost neutron orbit in $^{50}$Ca is not as small (large) as that of $^{80}$Ni, the $E1$ transition is suppressed. Therefore, the enhancement of the Coulomb

breakup cross section at $N > 28$ of the Ca isotopes is not so significant compared to that at $N > 50$ of the Ni isotopes.

## IV.  CONCLUSIONS

The low-lying $E1$ strength crucially depends on the shell structure near the Fermi surface. We have investigated the extent to which information on the $E1$ strength function of neutron-rich Ca, Ni, and Sn isotopes is imprinted on the total reaction cross sections. The nuclear breakup contributions are calculated based on the Glauber model with density distributions obtained by the Skyrme-Hartree-Fock+BCS method. The Coulomb multipole excitations of $E1$, $E2$, and $E3$ are also included with the use of the equivalent photon method (EPM), where the point-charge is replaced by the realistic finite-charge distribution and the strength function corresponding to the $E\lambda$ excitation is obtained by the canonical-basis-time-dependent-Hartree-Fock-Bogoliubov method.

No significant dependence of the $E1$ strength distribution appears with the small-$Z$ target, $^{40}$Ca, because the nuclear breakup cross section, which mostly reflects the matter radius, dominates in the total reaction cross section.

We have found that the low-lying $E1$ strength gives relatively large contribution to the total reaction cross section at the low-incident energy. At low-incident energy, the contributions of higher multipoles also get larger. In such a case, however, the neutron number dependence of the total reaction cross sections is still governed by the low-lying $E1$ strength because

the $E2$ and $E3$ contributions are not strongly dependent on the number of the neutrons, showing almost constant behavior. As the incident energy increases, the contribution from the strength in the giant dipole resonance region becomes large. The multipole excitations higher than $E1$ get small with increasing incident energy. With use of Pb target, the nuclear and Coulomb contributions of Sn isotopes become comparable and the $E1$ contribution is dominant at the incident energy higher than $500A$ MeV

With use of the larger-$Z$ targets, Sn and Pb, the difference of the Skyrme interaction or the shell structure near the Fermi surface can be seen clearly in the Coulomb breakup cross sections, which strongly depend on the excitation mechanism of the projectile and target nuclei. A comparison of the theory and experiment is desired to understand the shell structure of Ca, Ni, and Sn isotopes beyond $N = 28$, 50 and 82, respectively. Since the Coulomb breakup cross sections strongly depend on the low-lying $E1$ strength or the interaction employed at $N > 28$, 50, and 82 in the Ca, Ni, and Sn isotopes, respectively, it also gives strong constraint on the effective interaction.

In the present paper, we have discussed only spherical nuclei in which the $E2$ transitions are suppressed and change moderately on the neutron number. If the projectile nuclei exhibit different deformation, the $E2$ contribution may become large and changes significantly as a function of the neutron number. Further investigation for such systems is an interesting subject for future.

Our calculation of the Coulomb breakup cross section is performed on the basis of the EPM. Since the mutual Coulomb excitation of the projectile and target nuclei are treated independently in the present paper, its validity has to be tested by a comparison with experiment. Though our calculations agree with the few existing data, more data on accurate total reaction cross sections of nucleus-nucleus collisions are needed. As discussed in Ref. [52], the channel coupling effects becomes important in the Coulomb breakup process at the low-incident energy. It is certainly desirable to develop a consistent theory that can describe nucleus-nucleus inclusive Coulomb excitations.

## APPENDIX: EVALUATION OF EQ. (16)

The aim of this appendix is to carry out the integration in Eq. (16) for a finite-charge distribution. For $\rho_T(\boldsymbol{r})$ given as a superposition of Gaussians

$$\rho_T(\boldsymbol{r}) = \sum_i C_i e^{-a_i r^2}, \tag{A1}$$

the integration (16) is reduced to the following form:

$$\int d\boldsymbol{r}\, e^{i\frac{\omega}{v}z} e^{-ar^2} K_0\left(\left|\xi\left(\hat{\boldsymbol{b}}+\frac{1}{b}\boldsymbol{s}\right)\right|\right)$$
$$= 2\pi\sqrt{\frac{\pi}{a}}\frac{b^2}{\xi^2}\exp\left(-\frac{\omega^2}{4av^2}-ab^2\right)$$
$$\times \int_0^\infty dp\, p\, e^{-a\frac{b^2}{\xi^2}p^2} I_0\left(2a\frac{b^2}{\xi}p\right) K_0(p), \tag{A2}$$

and

$$\int d\boldsymbol{r}\, e^{i\frac{\omega}{v}z} e^{-ar^2} \widehat{\xi\left(\hat{\boldsymbol{b}}+\frac{1}{b}\boldsymbol{s}\right)} K_1\left(\left|\xi\left(\hat{\boldsymbol{b}}+\frac{1}{b}\boldsymbol{s}\right)\right|\right)$$
$$= 2\pi\sqrt{\frac{\pi}{a}}\frac{b^2}{\xi^2}\exp\left(-\frac{\omega^2}{4av^2}-ab^2\right)$$
$$\times \hat{\boldsymbol{b}} \int_0^\infty dp\, p\, e^{-a\frac{b^2}{\xi^2}p^2} I_1\left(2a\frac{b^2}{\xi}p\right) K_1(p), \tag{A3}$$

where $I_m$ is the $m$th order modified Bessel function of the first kind. The $p$-integration in Eqs. (A2) and (A3) can easily be done numerically.

[1] P.-G. Reinhard and W. Nazarewicz, Phys. Rev. C **81**, 051303(R) (2010).

[2] T. Inakura, T. Nakatsukasa, and K. Yabana, Phys. Rev. C **88**, 051305(R) (2013).

[3] X. Roca-Maza, X. Viñas, M. Centelles, B. K. Agrawal, G. Coló, N. Paar, J. Piekarewicz, and D. Vretenar, Phys. Rev. C **92**, 064304 (2015).

[4] S. Ebata, T. Nakatsukasa, and T. Inakura, Phys. Rev. C **90**, 024303 (2014).

[5] P. Papakonstantinou, H. Hergert, V. Yu. Ponomarev, and R. Roth, Phys. Rev. C **89**, 034306 (2014).

[6] P. Papakonstantinou, H. Hergert, and R. Roth, Phys. Rev. C **92**, 034311 (2015).

[7] T. Yamazaki et al., JHP Report (1986) (in Japanese).

[8] K. Ikeda, INS Report No. (1988) (in Japanese).

[9] Y. Suzuki, K. Ikeda, and H. Sato, Prog. Theor. Phys. **83**, 180 (1990).

[10] D. Mikami, W. Horiuchi, and Y. Suzuki, Phys. Rev. C **89**, 064303 (2014).

[11] T. Inakura, W. Horiuchi, Y. Suzuki, and T. Nakatsukasa, Phys. Rev. C **89**, 064316 (2014).

[12] T. Nakamura et al., Phys. Rev. Lett. **96**, 252502 (2006).

[13] T. Nakamura et al., Phys. Rev. Lett. **103**, 262501 (2009).

[14] B. Abu-Ibrahim and Y. Suzuki, Prog. Theor. Phys. **112**, 1013 (2004); **114**, 901 (2005).

[15] P. Capel, D. Baye, and Y. Suzuki, Phys. Rev. C **78**, 054602 (2008).

[16] M. Takechi et al., Mod. Phys. Lett. A **25**, 1878 (2010).

[17] R. Kanungo et al., Phys. Rev. C **83**, 021302(R) (2011).

[18] R. Kanungo et al., Phys. Rev. C **84**, 061304(R) (2011).

[19] M. Takechi et al., Phys. Rev. C **90**, 061305(R) (2014).

[20] K. Minomo, T. Sumi, M. Kimura, K. Ogata, Y. R. Shimizu, and M. Yahiro, Phys. Rev. C **84**, 034602 (2011).

[21] W. Horiuchi, T. Inakura, T. Nakatsukasa, and Y. Suzuki, Phys. Rev. C **86**, 024614 (2012).

[22] K. Minomo, T. Sumi, M. Kimura, K. Ogata, Y. R. Shimizu, and M. Yahiro, Phys. Rev. Lett. **108**, 052503 (2012).

[23] T. Sumi et al., Phys. Rev. C **85**, 064613 (2012).

[24] S. Watanabe *et al.*, Phys. Rev. C **89**, 044610 (2014).

[25] W. Horiuchi, Y. Suzuki, and T. Inakura, Phys. Rev. C **89**, 011601(R) (2014).

[26] W. Horiuchi, S. Hatakeyama, S. Ebata, and Y. Suzuki, Phys. Rev. C **93**, 044611 (2016).

[27] C. A. Bertulani and G. Baur, Phys. Rep. **163**, 299 (1988).

[28] Y. Suzuki, R. G. Lovas, K. Yabana, and K. Varga, *Structure and Reactions of Light Exotic Nuclei* (Taylor & Francis, London, 2003).

[29] C. A. Bertulani and P. Danielewicz, *Introduction to Nuclear Reactions*, Graduate Student Series in Physics (CRC-Taylor & Francis, London, 2004).

[30] W. Horiuchi, Y. Suzuki, P. Capel, and D. Baye, Phys. Rev. C **81**, 024606 (2010).

[31] M. Yahiro, K. Ogata, and K. Minomo, Prog. Theor. Phys. **126**, 167 (2011).

[32] K. Yoshida, T. Fukui, K. Ogata, and K. Minomo, Prog. Theor. Exp. Phys. **2014**, 053D03 (2014).

[33] B. Abu-Ibrahim and Y. Suzuki, Phys. Rev. C **62**, 034608 (2000).

[34] R. J. Glauber, in *Lectures in Theoretical Physics*, edited by W. E. Brittin and L. G. Dunham (Interscience, New York, 1959), Vol. 1, p. 315.

[35] B. Abu-Ibrahim and Y. Suzuki, Phys. Rev. C **61**, 051601(R) (2000).

[36] B. Abu-Ibrahim, W. Horiuchi, A. Kohama, and Y. Suzuki, Phys. Rev. C **77**, 034607 (2008).

[37] W. Horiuchi and Y. Suzuki, Phys. Rev. C **74**, 034311 (2006).

[38] W. Horiuchi, Y. Suzuki, B. Abu-Ibrahim, and A. Kohama, Phys. Rev. C **75**, 044607 (2007).

[39] B. Abu-Ibrahim, S. Iwasaki, W. Horiuchi, A. Kohama, and Y. Suzuki, J. Phys. Soc. Jpn. **78**, 044201 (2009).

[40] J. Bartel, P. Quentin, M. Brack, C. Guet, and H. Håkansson, Nucl. Phys. A **386**, 79 (1982).

[41] E. Chabanat, P. Bonche, P. Haensel, J. Meyer, and R. Schaeffer, Nucl. Phys. A **627**, 710 (1997).

[42] P.-G. Reinhard and H. Flocard, Nucl. Phys. A **584**, 467 (1995).

[43] S. Ebata and T. Nakatsukasa, Phys. Scr. **92**, 064005 (2017).

[44] A. Bohr and B. R. Mottelson, *Nuclear Structure*, Vol. I (W. A. Benjamin, New York, 1975).

[45] S. Ebata, T. Nakatsukasa, T. Inakura, K. Yoshida, Y. Hashimoto, and K. Yabana, Phys. Rev. C **82**, 034306 (2010).

[46] T. Nakatsukasa and K. Yabana, Phys. Rev. C **71**, 024301 (2005).

[47] C. A. Bertulani and A. M. Nathan, Nucl. Phys. A **554**, 158 (1993).

[48] A. Bohr and B. R. Mottelson, *Nuclear Structure*, Vol. II (W. A. Benjamin, New York, 1975).

[49] P. Ring and P. Schuck, *The Nuclear Many-Body Problem* (Springer-Verlag, New York, 1980).

[50] S. Kox *et al.*, Phys. Rev. C **35**, 1678 (1987); J. F. Bruandet, J. Phys. (Paris) Colloq. **47**, C4-125 (1986).

[51] E. Lipparini and S. Stringari, Phys. Rep. **175**, 103 (1989).

[52] N. S. Brady, T. Aumann, C. A. Bertulani, and J. O. Thomas, Phys. Lett. B **757**, 553 (2016).